Counterion-Dependent Access to Low Symmetry Lyotropic Sphere Packings of Ionic Surfactant Micelles

*Ashish Jayaraman and Mahesh K. Mahanthappa**

Department of Chemical Engineering & Materials Science, 421 Washington Ave., SE, University of Minnesota, Minneapolis, MN 55455

* Email: maheshkm@umn.edu; +1 (612) 625-4599

ORCID

Mahesh K. Mahanthappa: 0000-0002-9871-804X

Ashish Jayaraman: 0000-0001-7071-7419

KEYWORDS liquid crystals • self-assembly • surfactants • micelles • Frank–Kasper phases • lyotropic phases • X-ray scattering

Abstract

The water-driven self-assembly of homologous dianionic surfactants into lyotropic liquid crystals (LLCs) is investigated, with a focus on understanding how surfactant headgroup and counterion identities guide supramolecular spherical mesophase selection. Using temperature-dependent small-angle X-ray scattering (SAXS), we demonstrate that 2-alkylmalonate surfactants (**C_nMal-M_2**) with *n* = 8 (octyl) or 10 (decyl) and M = K^+, Cs^+ or $(CH_3)_4N^+$ form both simple and complex micelle packings. Observed spherical morphologies include body-centered cubic (BCC), hexagonally closest-packed (HCP), and tetrahedrally closest-packed Frank-Kasper (FK) A15 and σ phases (*Pm3(-)n* and *$P4_2/mnm$* symmetries, respectively). Previously observed in only one other minimally hydrated surfactant, the σ phase is a rare LLC morphology comprising a low symmetry unit cell containing 30 sub-2 nm quasispherical micelles, each of which belongs to one of five symmetry-equivalent classes with discrete aggregation numbers. Temperature versus water concentration phase maps for **C_nMal-M_2** LLCs reveal that σ phase formation depends sensitively on the size and polarizability of the surfactant counterion, and the length of the surfactant alkyl tail. These observations are rationalized in terms of a delicate interplay between global packing symmetry and local particle symmetry, and the extent to which counterion-headgroup correlations enforce the latter structures in these LLC phases.

Introduction

Amphiphilic molecules, comprising polar headgroups covalently linked to non-polar hydrocarbon tails, self-assemble in water to minimize unfavorable hydrophobic/water contacts while optimizing headgroup hydration.[1] The myriad of useful properties of these hydrated materials stem from the specific morphologies of their supramolecular assemblies, which include spherical and worm-like micelles and bilayer vesicles.[2] Aqueous dispersions of worm-like micelles find widespread applications as rheological modifiers in diverse contexts, including enhanced oil recovery and personal care product formulations due to their viscoelastic properties.[3-5] Spherical micelles and vesicular structures also find applications as stabilizers and encapsulation agents in therapeutic delivery applications.[6-9] The non-covalent assemblies formed by hydrated surfactants delicately balance the interfacial tension between the hydrophilic and hydrophobic domains against steric and electrostatic repulsions between the hydrophilic headgroups.[10-13]

The self-assembled structures formed by ionic surfactants depend sensitively on the structures of their hydrophobic tails, the counterion-headgroup pair chemistries, and the extent of their hydration.[11, 13-15] Highly dissociated surfactant counterions induce electrostatic repulsions between adjacent headgroups situated at the hydrophobic/hydrophilic interface, leading to the formation of high curvature spherical micelles.[16] On the other hand, counterion association with the interfacial headgroups mitigates such electrostatic repulsions and enables formation of flatter curvature aggregates such as cylindrical micelles, bilayers (lamellae) and vesicles.[17, 18] However, the hydrated headgroup arrangements must also allow packing of the surfactant hydrocarbon tails at nearly constant density while minimizing their unfavorable interactions with water.[14, 15] At low hydrations when the surfactant counterion and headgroup are closely associated, the interfacial tension between the "salty" aqueous and hydrophobic domains is high. Thus, the surfactant tails stretch away from the interface in a manner that leads to tight intermolecular packings into low mean curvature aggregates. If instead the counterion and headgroup are highly dissociated, then the interfacial tension between the hydrophobic and hydrophilic domains is lower and highly curved spherical micelles form.[19, 20] Thus, judicious pairing of headgroup-counterion chemistry with hydrocarbon tail structure offers opportunities for subtly tuning the preferred interfacial curvatures of these supramolecular structures and their consequent properties.[14]

At low surfactant concentrations in water above the critical micelle concentration, dielectric screening of interactions between micelles results in the absence of long-range intermicellar correlations. Dehydrating these micellar dispersions beyond a critical concentration leads the counterion clouds around the micelles to impinge and to induce cohesion, resulting in formation of lyotropic liquid crystals (LLCs). LLCs are supramolecular assemblies that exhibit periodic nanoscale order, the morphologies of which depend upon the concentration, temperature, and pressure at which they form.[21-24] Well-known LLC morphologies include lamellae (L_α), bicontinuous network phases (N), hexagonally-packed cylinders (H), and spherical micelle packings (I). In a manner similar to the dilute solution phase behavior of ionic amphiphiles, the self-assembled structures of LLCs primarily reflect the chemical structure of the surfactant, the degree of its solvation, and temperature. LLCs are classified by the curvature of their hydrophobic domains: Type I LLCs exhibit convex hydrophobic interfaces, whereas the hydrophobic domains are concave in Type II structures.[25] The hydrophilic/hydrophobic domain interfaces in these nanostructured assemblies are lined with the surfactant headgroups and their counterions, which endow them with unique properties. H- and N-phase LLCs have found applications as water purification membranes,[26, 27] structured ion-conducting electrolytes,[28, 29] templates for mesoporous materials syntheses,[30-33] and therapeutic delivery vehicles.[6, 8, 9, 34]

A recent review by Shearman *et al*. cataloged the bewildering array of LLC sphere packings observed to date.[35] By analogy to colloidal hard sphere packings and metallic crystals,[36] micelles can self-assemble into high symmetry body-centered cubic (BCC), high packing fraction face-centered cubic (FCC) and hexagonally closest-packed (HCP) LLC spheres phases. However, the deformability of soft spheres also enables deviations from their preferred spherical particle symmetries, which facilitate their packing into complex, low symmetry phases.[37, 38] For example, Balmbra *et al*. first reported a Type I cubic micellar LLC packing with *Pm3(-)n* symmetry.[39] Vargas *et al*. later elucidated the structure of this complex Type I phase[40] as a tetrahedral close packing of two spherical and six platelet micelles into a cubic unit cell, which mimics that of the Cr_3Si intermetallic A15 structure.[36] In Type I LLCs, A15, FCC, BCC, and HCP sphere packings are well documented.[35] Pioneering work by Seddon and co-workers has also established that certain natural lipids form Type II aqueous LLCs with *Fd3(-)m* symmetry.[41, 42] The latter structure has eight reverse micelles situated at the positions of a cubic diamond lattice, wherein the remaining tetrahedral interstitial sites are filled with tetrahedral groupings of smaller reverse micelles. This so-called C15 phase mimics the $MgCu_2$ intermetallic structure.[36] We note that the *Fd3(-)m* structure is ubiquitous in Type II LLCs, with only relatively recent reports of inverse FCC,[43] HCP,[44] and A15[45] phases. Notable common features of both of the A15 and C15 LLC sphere packings include the formation of giant, low symmetry unit cells containing ≥ 8 micelles of different and discrete volumes.

The aforementioned micellar LLC sphere packings belong to a broader class of tetrahedrally close packed structures known as Frank-Kasper (FK) phases, which were first identified over 50 years ago in metals and their alloys.[46] A defining feature of these complex, low symmetry phases is that their lattice sites exhibit either 12-, 14-, 15- or 16-fold coordination.[47] Thus, the aforementioned A15 and C15 LLCs represent the first examples of FK phases observed in soft materials, and until recently, these were the only FK LLC phases known. Over the last 15 years, FK phases have been observed in “amphiphilic” systems in the absence of solvents, including thermotropic liquid crystals based on wedge-type dendrons,[48-50] in giant shape amphiphiles,[51-53] and in linear diblock and multiblock polymers.[54-57] Percec, Ungar, and co-workers have elucidated the detailed structures of the FK phases formed by families of wedge-type dendrons using electron microscopy and X-ray diffraction.[58-64] These phases are recognized as periodic 3D approximants of quasicrystals.[65, 66] Quasicrystals exhibit local rotational symmetry, yet they are devoid of long-range translational order.[67] By virtue of these structural relationships, dodecagonal QCs have been observed in these “amphiphilic” self-assembled materials,[53, 54, 68-70] and in micellar solutions of non-ionic diblock polymers.[71]

Kim *et al*. only very recently reported that hydration of bis(tetramethylammonium) decylphosphonate (**DPA-TMA$_2$**) drives the formation of an exceptionally well-ordered and previously unknown Type I FK σ LLC phase with $P4_2/mnm$ symmetry (Figure 1).[72] The lyotropic σ mesophase exhibits a large, low symmetry unit cell containing 30 quasispherical micelles, which belong to five different symmetry-equivalent classes each with discrete aggregation numbers. This unusual structure, which mimics that of *β*-tantalum, *β*-uranium, and $Fe_{46}Cr_{54}$ alloys,[36] represents the LLC analog of previously reported thermotropic dendron and block polymer phases.[50, 56] The formation of FK σ phases in wedge-type dendrons and block polymers and conceptually related Type II C15 LLCs has been argued to stem from filling space with uniform density, while maximizing the spherical symmetry of the inverse micelles.[73, 74] In other words, these amphiphilic materials adopt structures that minimize differential molecular stretching known as "packing frustration" or "lipid tail frustration" within the hydrocarbon matrix phase.[74-77] In Type II LLCs, it is known that the addition of hydrophobic additives can relieve packing frustration and enable access to other phases.[43] However, such arguments do not apply to Type I LLCs, in which the normal micelles surrounded by water make no van der Waals contacts. Kim *et al*. instead rationalized the formation of Type I FK A15 and σ phases as maximizing electrostatic cohesion between the micelles, while minimizing variations in surfactant counterion-headgroup hydration.[72] Since only one example of a FK LLC σ phase has been reported to date, amphiphile design criteria that facilitate reliable access to these structurally complex packings are unknown.

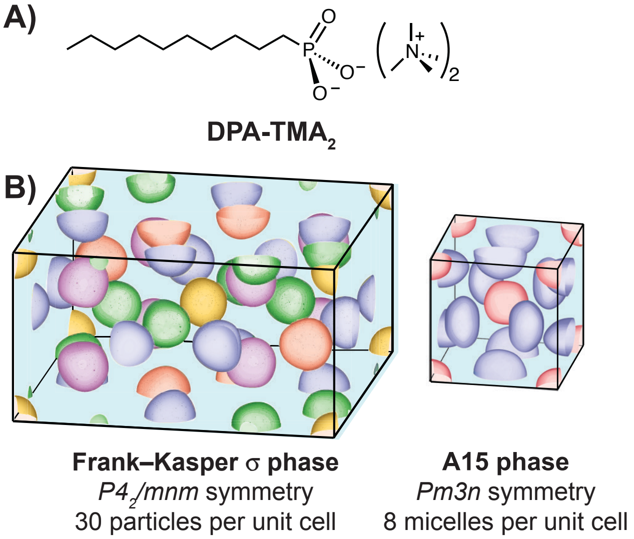

Figure 1. (A) Chemical structure of the dianionic surfactant **DPA-TMA$_2$**, which (B) forms tetrahedrally close packed aqueous lyotropic Frank-Kasper σ and A15 mesophases. In the low symmetry σ phase unit cell that contains 30 particles, five discrete micelle sizes spontaneously form to maximize electrostatic cohesion in the LLC while minimizing variations in surfactant hydration.

In this report, we investigate the synthesis and aqueous LLC phase behaviors of dianionic surfactants in order to identify molecular motifs that drive formation of complex FK mesophases. Our studies focus on homologous 2-alkylmalonate surfactants (**C$_n$Mal-M$_2$**), in which the dicarboxylate headgroups carry charge-compensating counterions M = K^+, Cs^+ or $(CH_3)_4N^+$ (TMA^+). By mapping the water concentration-dependent LLC phase behaviors of these amphiphiles using temperature-dependent X-ray scattering, we demonstrate that access to the FK σ phase crucially depends on the nature of the counterion and the degree of its dissociation from the dianionic surfactant headgroups. Soft and highly dissociated counterions enable σ phase formation, while more closely associated ion pairs instead favor surfactant self-assembly into FK A15 phases. The length of the alkyl chain exerts a weaker influence over the preferred LLC structures, although shorter alkyl surfactant tails also favor σ phase formation. Thus, these studies provide new insights into amphiphile structures that stabilize FK σ phase LLCs.

Experimental Section

Materials. All reagent grade solvents and chemicals were purchased from the Sigma–Aldrich Chemical Co. (Milwaukee, WI) and used as received unless otherwise noted. Lauric acid was obtained from Acros Organics (Geel, Belgium) and used as received. Anhydrous, anaerobic tetrahydrofuran (THF) was obtained by sparging analytical grade solvent with $N_2(g)$ for 30 min, followed by repetitive circulation through a column of activated molecular sieves over 12 h in a Vacuum Atmospheres Co. (Hawthorne, CA) solvent purification system. Hexamethylphosphoramide (HMPA) and diisopropylamine ($i\mathrm{Pr}_2\mathrm{NH}$) were distilled from CaH_2 and stored under nitrogen. *n*-Butyllithium (2.154 M in hexanes) was titrated using $Ph_2CHCOOH$ acid in anhydrous and anaerobic THF prior to use. $(CH_3)_4NOH(aq)$ was titrated against a standardized solution of 1 N $HCl(aq)$ and thus determined to have a concentration of 0.9912 M aqueous base.

Molecular Characterization. ^{1}H and ^{13}C nuclear magnetic resonance (NMR) spectra were recorded on a Bruker Avance III HD 400 MHz spectrometer with Smartprobe or an Bruker Avance III HD 500 MHz spectrometer with a TCI cryoprobe. All spectra were obtained in and were referenced relative to the residual proton shift in CD_3OD (δ 3.31 ppm) or DMSO-d_6 (δ 2.50 ppm). Carbon/Hydrogen/Nitrogen (C/H/N) combustion elemental analyses were performed by Atlantic Microlab, Inc. (Norcross, GA, USA).

Representative Synthesis of 2-Octylmalonic Acid (C_8Mal). This synthetic protocol was adapted from that of Weber and Mahanthappa.[78] A 500 mL 2-neck round bottom flask fitted with an addition funnel and equipped with a stir bar was charged with $i\mathrm{Pr}_2\mathrm{NH}$ (16.73 mL, 119.0 mmol) and THF (30 mL) under a nitrogen atmosphere. This solution was cooled to -40 °C in an $EtOH/H_2O/CO_2(s)$ bath and *n*-BuLi (44.8 mL, 116 mmol) was added dropwise via addition funnel, whereupon the solution turned pale yellow. After stirring this reaction mixture for 30 min, a solution of decanoic acid (9.998 g, 58.04 mmol) in THF (60 mL) was added dropwise via addition funnel. HMPA (10.0 mL, 57.5 mmol) was subsequently added, and the stirred reaction mixture was warmed to 22 °C and stirred for 30 min. The resulting enolate solution was again cooled to -40 °C and it was transferred batchwise via cannula to a 500 mL 2-neck round bottom flask containing excess CO_2(*s*) (> 255 g, > 5.79 mol) under a nitrogen atmosphere over 45 min. The reaction mixture was then allowed to warm slowly to 22 °C over 12 h, leading to soft gel formation. This gelatinous reaction mixture was quenched by the addition of 2.0 M HCl (60 mL), which yielded two distinct layers. The layers were separated and the aqueous (lower) layer was washed with diethyl ether (3 × 50 mL). The combined organic layers were washed with 2.0 M HCl (3 × 25 mL) followed by saturated NaCl (*aq*) (2 × 25 mL). The ether layer was then dried using $MgSO_4$(*s*) and concentrated under vacuum to yield a white solid. The crude product was purified by recrystallization from heptane (100 mL), and the resulting crystals were azeotropically freeze-dried from C_6H_6 prior to further use. Yield: 8.29 g (66.0%) ^{1}H NMR: (500 MHz, DMSO-d_6, 22 °C) δ (ppm): 12.61 (COO*H*, *s*, 2H), 3.17 (C*H*, *t*, 1H), 1.70 (CH-CH_2-CH_2, *q*, 2H), 1.24 (CH_2, *m*, 12H), 0.86 (CH_3-CH_2, *t*, 3H) ^{13}C NMR: (126 MHz, DMSO-d_6, 22 °C) δ (ppm): 171.35 (C=O), 52.05 (CH), 31.71 (CH_2), 29.23 (CH_2), 29.20 (CH_2), 29.06 (CH_2), 28.83 (CH_2), 22.55 (CH_2), 14.37 (CH_3).

2-Decylmalonic Acid (C_{10}Mal). Synthesized from lauric acid and CO_2(*s*) per the procedure for **C_8Mal**. Yield: 9.63 g (78.9%) ^{1}H NMR: (500 MHz, DMSO-d_6, 22 °C) δ (ppm): 12.61 (COO*H*, *s*, 2H), 3.18 (C*H*, *t*, 1H), 1.70 (CH-CH_2-CH_2, *q*, 2H), 1.24 (CH_2, *m*, 16H), 0.86 (CH_3, *t*, 3H) ^{13}C NMR: (126 MHz, DMSO-d_6, 22 °C) δ (ppm): 171.35 (C=O), 52.05 (CH), 31.77 (CH_2), 29.45 (CH_2), 29.42 (CH_2), 29.29 (CH_2), 29.21 (CH_2), 29.19 (CH_2), 28.84 (CH_2), 27.27 (CH_2), 22.57 (CH_2), 14.38 (CH_3).

Representative Synthesis of Tetramethylammonium 2-Octylmalonate (C_8Mal-TMA$_2$). 2-octylmalonic acid (1.00 g, 4.63 mmol) and $(CH_3)_4NOH$(*aq*) (9.50 mL of 0.9912 M solution, 9.42 mmol) were suspended in CH_3OH at a concentration of 0.15 M and stirred for 12 h. The reaction mixture was filtered through a fine glass frit, and the filtrate was concentrated *in vacuo* to furnish a quantitative yield of a white solid. Hygroscopic solids thus obtained were freeze–dried three times from C_6H_6, and stored in a glove box under an argon atmosphere to avoid adventitious atmospheric moisture uptake. ^{1}H NMR (400 MHz, CD_3OD, 22 °C) δ (ppm): 3.21 (N-CH_3, *s*, 24H), 3.11 (C*H*, *t*, 1H), 1.85 (CH-CH_2-CH_2, *m*, 2H), 1.31 (C*H*$_2$, *m*, 12H), 0.91(C*H*$_3$-CH$_2$, *t*, 3H). ^{13}C NMR: (101 MHz, CD$_3$OD, 22 °C) δ (ppm): 180.07 (C=O), 60.80 (CH), 55.99 (N-*C*H$_3$, *t*), 33.09 (CH$_2$), 32.58 (CH$_2$), 31.13 (CH$_2$), 30.89 (CH$_2$), 30.52 (CH$_2$), 30.02 (CH$_2$), 23.74 (CH$_2$), 14.48 (CH$_3$). *Anal.* Calc: $C_{19}H_{42}O_4N_2 \bullet 0.88\ H_2O$: C, 60.29; H, 11.68; N, 7.40; Found: C, 60.29; H, 11.85; N, 7.29.

Potassium 2-octylmalonate (C_8Mal-K_2). Synthesized from 2-octylmalonic acid and K_2CO_3(*s*) in place of $(CH_3)_4NOH$ per the above protocol. ^{1}H NMR (400 MHz, CD$_3$OD, 22 °C) δ (ppm): 3.09 (C*H*, *t*, 1H), 1.82 (CH-C*H*$_2$-CH$_2$, *m*, 2H), 1.31 (C*H*$_2$, *m*, 12H), 0.91(C*H*$_3$-CH$_2$, *t*, 3H). ^{13}C NMR: (101 MHz, CD$_3$OD, 22 °C) δ (ppm): 181.08 (C=O), 60.52 (CH), 33.08 (CH$_2$), 32.32 (CH$_2$), 31.01 (CH$_2$), 30.82 (CH$_2$), 30.49 (CH$_2$), 29.91 (CH$_2$), 23.72 (CH$_2$), 14.45 (CH$_3$). *Anal.* Calc: $C_{11}H_{18}O_4K_2 \bullet 0.28\ H_2O$: C, 44.39; H, 6.30; Found: C, 44.39; H, 6.26.

Cesium 2-octylmalonate (C_8Mal-Cs_2). Synthesized from 2-octylmalonic acid and Cs_2CO_3(*s*) in place of $(CH_3)_4NOH$ per the above protocol. ^{1}H NMR (400 MHz, CD$_3$OD, 22 °C) δ (ppm): 3.08 (C*H*, *t*, 1H), 1.82 (CH-C*H*$_2$-CH$_2$, *m,* 2H), 1.31 (C*H*$_2$, *m*, 12H), 0.91(C*H*$_3$-CH$_2$, *t*, 3H). ^{13}C NMR: (101 MHz, CD$_3$OD, 22 °C) δ (ppm): 180.70 (C=O), 60.37 (CH), 33.09 (CH$_2$), 32.25 (CH$_2$), 31.02 (CH$_2$), 30.83 (CH$_2$), 30.50 (CH$_2$), 29.89 (CH$_2$), 23.74 (CH$_2$), 14.45 (CH$_3$). *Anal.* Calc: $C_{11}H_{18}O_4Cs_2 \bullet 0.46\ H_2O$: C, 27.05; H, 3.91; Found: C, 27.05; H, 4.25.

Tetramethylammonium 2-decylmalonate (C_{10}Mal-TMA$_2$). ^{1}H NMR (400 MHz, CD$_3$OD, 22 °C) δ (ppm): 3.12 (N-C*H*$_3$, *s*, 24H), 3.1 (C*H*, *t*, 1H), 1.85 (CH-C*H*$_2$-CH$_2$, *m*, 2H), 1.31 (C*H*$_2$, *m*, 16H), 0.91 (C*H*$_3$-CH$_2$, *t*, 3H). ^{13}C NMR: (101 MHz, DMSO-d_6, 22 °C) δ (ppm): 180.10 (C=O), 60.82 (CH), 55.98 (N-*C*H$_3$, *t*), 33.07 (CH$_2$), 31.13 (CH$_2$), 30.93 (CH$_2$), 30.86 (CH$_2$), 30.79 (CH$_2$), 30.48 (CH$_2$), 30.02 (CH$_2$), 23.74 (CH$_2$), 14.47 (CH$_3$). *Anal.* Calc: $C_{21}H_{46}O_4N_2 \bullet 0.89\ H_2O$: C, 62.00; H, 11.86; N, 6.89; Found: C, 62.00; H, 12.07; N, 7.00.

Cesium 2-decylmalonate (C_{10}Mal-Cs_2). ^{1}H NMR (400 MHz, CD$_3$OD, 22 °C) δ (ppm): 3.09 (C*H*, *t*, 1H), 1.82 (CH-C*H*$_2$-CH$_2$, *m*, 2H), 1.31 (C*H*$_2$, *m*, 12H), 0.91(C*H*$_3$-CH$_2$, t, 3H). ^{13}C NMR: (101 MHz, DMSO-d_6, 22 °C) δ (ppm): 180.66 (C=O), 60.28 (CH), 33.08 (CH$_2$), 32.25 (CH$_2$), 31.01 (CH$_2$), 30.86

(CH_2), 30.83 (CH_2), 30.78 (CH_2), 30.48 (CH_2), 29.97 (CH_2), 23.74 (CH_2), 14.46 (CH_3). *Anal*. Calc: $C_{13}H_{22}O_4Cs_2$ • 1.18 H_2O: C, 29.49; H, 4.65; Found: C, 29.49; H, 4.52.

Lyotropic Liquid Crystal (LLC) Sample Preparation. LLC samples were prepared by massing desired amounts of surfactant into 1 dram vials, followed by the addition of ultra-pure water (18 MΩ•cm). These mixtures were homogenized to yield clear gel-like solids by three cycles of centrifugation (4950 × g for 10 min) and hand-mixing. Sample vials were capped and sealed with Parafilm to prevent any loss of water. Binary surfactant/H_2O LLC compositions are reported in terms of w_{0_s} = (total mol H_2O)/(mol surfactant), wherein the numerator in this quotient accounts for both the added water and that arising from the surfactant hydrate.

Small- and Wide-angle X-Ray Scattering (SWAXS): LLC sample morphologies were investigated using synchrotron SWAXS analyses. Using an incident beam energy of 13.3 keV ($\lambda = 0.932$ Å) and a 2.027 m sample-to-detector distance at the 12-ID-B beamline of the Advanced Photon Source (Argonne, IL), synchrotron 2D-SWAXS patterns were recorded on a Pilatus 2M (25.4 cm × 28.9 cm rectangular area) detector with 1475 × 1679 pixel resolution (172 μm x 172 μm pixel size). The scattering wavevector (q) scale in these patterns was calibrated using a silver behenate standard ($d = 58.38$ Å). LLC samples were hermetically sealed in alodined aluminum DSC pans (TA Instruments, Newcastle, DE), which were equilibrated at the desired temperature using a home-built multi–array sample stage for at least 5 min prior to SWAXS analysis (typical exposure times ≤ 0.1 s). SWAXS patterns were obtained in the first heating cycle of the LLC samples as prepared, with additional patterns acquired at 25 °C upon completion of the temperature sweep to assess potential phase metastability. Unless otherwise noted in the text, the initial and final LLC phases were identical upon thermal cycling. The resulting 2D patterns were azimuthally-integrated to obtain one-dimensional scattered intensity $I(q)$ versus q plots, using the DataSqueeze software package (http://www.datasqueezesoftware.com/).

Using the *JANA2006* crystallographic computing system software,[79] Le Bail refinement of selected SWAXS data sets was used to extract the structure factor intensities for each scattering maximum.

These data were used as inputs for the charge flipping algorithms within the *SUPERFLIP* software package[80] to reconstruct the electron density maps for various observed LLC phases. The resulting electron density contour maps (typically, 90% isosurfaces) were visualized using the VESTA software package,[81] from which electron density line profiles along selected crystallographic directions were obtained. Details of these analyses along with the *SUPERFLIP* input files (in which the static structure factor intensities are listed) are provided in the Supporting Information.

Results and Analysis

Given the recent discovery of an aqueous LLC σ mesophase in the dianionic surfactant **DPA-TMA$_2$**,[72] we sought to identify amphiphile design criteria that enable robust access to this and other low symmetry lyotropic packings of ionic micelles. Based on the structure of **DPA–TMA$_2$**, we initially sought to assess whether a dianionic surfactant headgroup was an essential ingredient for σ phase formation and whether its chemical identity influences the stability of this complex packing. Additionally, we aimed to probe the extent to which the charge–compensating counterions guide LLC phase selection. Consequently, we synthesized a series of analytically pure 2-alkylmalonate surfactants with *n*-octyl and *n*-decyl tails by the method of Weber *et al.*[78] (Scheme 1), in which the carboxylate head groups bear either K^+, Cs^+ or $(CH_3)_4N^+$ (TMA^+) counterions. Hereafter, we designate the surfactants **C$_n$Mal-M$_2$**, where *n* is the total number of carbons in the alkyl chain appended to the 2-position of the malonate headgroup and M^+ = TMA^+, Cs^+, and K^+ is the surfactant counterion. Note that there are always two monovalent counterions (M^+) associated with each malonate headgroup to maintain charge neutrality. We restricted our attention to monovalent counterions to avoid potential surfactant precipitation through the formation of bridging interactions between headgroups fostered by divalent counterions.[82] Note that Hagslaett *et al.* previously studied the aqueous LLC phase behavior of related dipotassium dodecylmalonate surfactants, however, the quality of their SAXS data was insufficient to conclusively identify the observed morphologies.[16]

Scheme 1. Synthesis of 2-Alkylmalonates Surfactants.

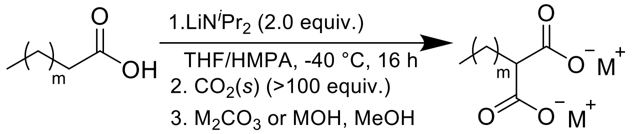

C_8Mal-TMA$_2$: m = 7, $M^+ = (CH_3)_4N^+$
C_8Mal-K$_2$: m = 7, $M^+ = K^+$
C_8Mal-Cs$_2$: m = 7, $M^+ = Cs^+$
C_{10}Mal-TMA$_2$: m = 9, $M^+ = (CH_3)_4N^+$
C_{10}Mal-Cs$_2$: m =9, $M^+=Cs^+$

The aqueous LLC phase behavior of **C_{10}Mal-TMA$_2$** was investigated by SWAXS analyses of a series of samples with surfactant headgroup hydrations ranging from w_{0_s} = (total mol H_2O)/(mol surfactant) = 3–40 (Figure 2). All SWAXS patterns were acquired during the first heating cycle of the as prepared LLC samples, and patterns were obtained upon cooling to 25 °C to assess potential metastability of the observed phases. Samples with $w_{0_s} > 40$ form free flowing solutions of disordered micelles. In the headgroup hydration range $24 \leq w_{0_s} \leq 37$, we observe an ordered LLC phase with an ambient temperature SWAXS signature comprising at least 12 peaks corresponding to hexagonally closest-packed (HCP) spherical micelles. A representative azimuthally-integrated SWAXS intensity profile for this HCP LLC obtained at 25 °C with $w_{0_s} = 25.9$ (Figure 2A) exhibits unit cell parameters $a \approx 3.94$ nm and $c \approx 6.42$ nm. The observed $c/a = 1.629$ deviates modestly from the ideal value of 1.635, which is geometrically predicted for HCP hard spheres. The scattering signature for this sample, including the slightly diminished intensity of the (002) scattering peak ($q = 0.1958$ Å^{-1}), is similar to that reported by Liu and Warr for LLCs of cationic 4° ammonium surfactants with strongly hydrated counterions.[83] Upon heating this sample to 60 °C, we observe a transition to a body-centered cubic (BCC) sphere packing, evidenced by the observation of up to six SWAXS maxima at relative positions $q/q^* = \sqrt{2}, \sqrt{4}, \sqrt{6}, \sqrt{10}, \sqrt{12}$ and $\sqrt{14}$ ($q^* = 0.2057$ Å^{-1}). These peaks correspond to the (110), (200), (211), (310), (222), and (321) Miller planes of a supramolecular BCC structure, with a (220) peak extinction. When $T > 80$ °C, the sharp peaks for the ordered BCC LLCs melt into the broad intermicellar correlation scattering associated with a disordered dispersion of micelles. In the hydration window w_{0_s} = 38–40, we observe formation of an ordered BCC micelle packing that coexists with disordered micelles. The occurrence of a BCC phase near the lyotropic order-disorder transition hydration ($w_{0_s,\mathrm{ODT}}$) is anticipated by the entropic arguments of Alexander and McTague regarding liquid-solid phase transitions: the configurational entropy loss upon symmetry breaking of the liquid state to form an ordered LLC is minimized by formation of a BCC phase due to site symmetry equivalence within this lattice.[84] Across the window w_{0_s} = 24–40, the thermal order-disorder transition temperature (T_{ODT}) monotonically decreases with increasing w_{0_s}.

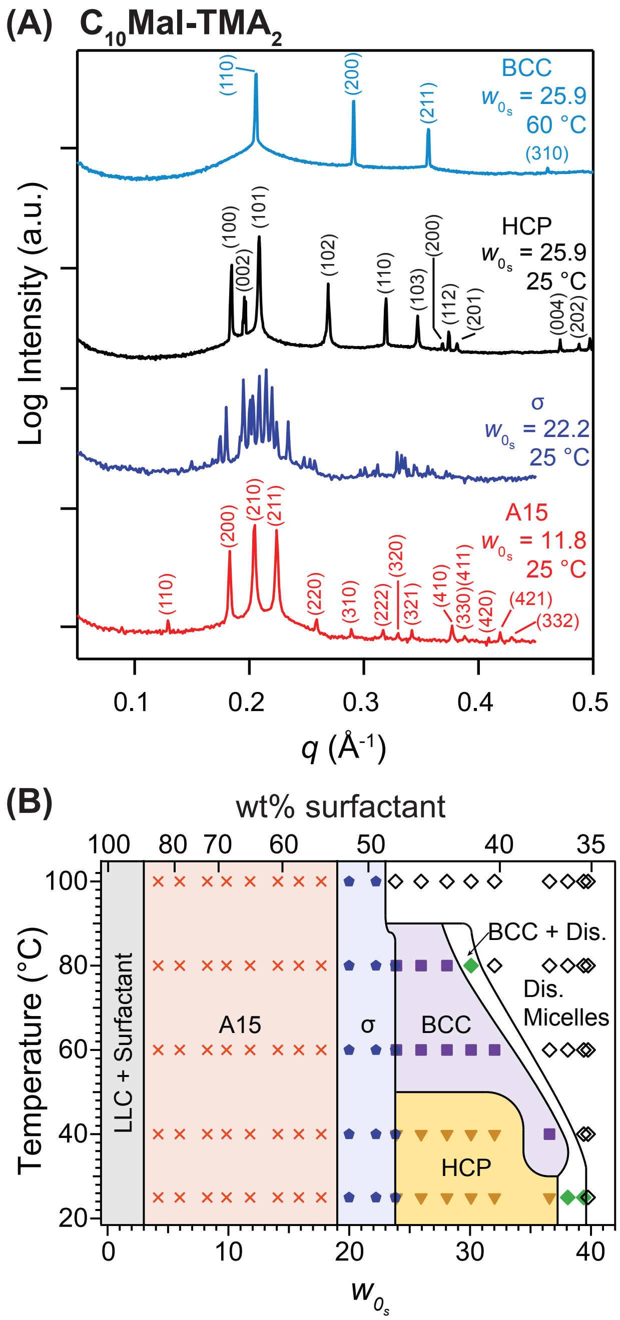

Figure 2. Aqueous lyotropic liquid crystalline phase behavior for **C_{10}Mal-TMA$_2$**. (A) Synchrotron SWAXS powder patterns illustrating the formation of A15, σ, HCP and BCC ordered phases at various headgroup hydration numbers w_{0_s}. (B) Temperature versus w_{0_s} phase diagram depicting the lyotropic mesophase progression of ordered phases to disordered micellar solutions with increasing w_{0_s}.

In the headgroup hydration range w_{0_s} = 20–24, **C_{10}Mal-TMA$_2$** forms a LLC characterized by the appearance of at least 40 instrument resolution-limited SWAXS peaks (Figure 2A). This distinctive scattering signature conforms to that previously reported for FK σ phases ($P4_2/mnm$ symmetry) of LLCs and block polymers.[56, 72] Detailed analyses of a SWAXS pattern obtained at w_{0_s} = 22.2 at 25 °C demonstrate the formation of a giant tetragonal unit cell with a = 13.3 nm and c = 6.99 nm (c/a = 0.526), constituting only the second report of a LLC FK σ phase (see Figure S1 for fully indexed pattern and Table S1 for complete listing of peaks positions and residuals). Based on the observation of various high index peaks (*e.g.*, (730)) in conjunction with the unit cell parameter, we estimate that the coherent grain radii for these LLCs comprising sub-2 nm micelles exceed ~90 nm. As in the case of the LLC FK σ phase derived from **DPA-TMA$_2$**, this LLC structure is characterized by exceptional long-range translational order at length scales that are somewhat unusual in lyotropic mesophases.[72, 85] We note that the unit cell parameters for the σ phase based on **C$_{10}$Mal-TMA$_2$** are comparable to those reported for the same phase derived from the ten-carbon surfactant **DPA-TMA$_2$**, suggesting similarities in their packings and mechanisms of complex phase formation.

At the lower hydrations w_{0_s} = 3–19, we found that **C$_{10}$Mal-TMA$_2$** forms aqueous LLCs exhibiting much simpler scattering patterns with up to 14 SWAXS peaks located at q/q^* = √2, √4, √5, √6, …etc. (Figure 2A). These peak positions are consistent with a FK A15 phase with cubic *Pm3(-)n* space group symmetry, which has been previously observed in other ionic surfactant LLCs.[40, 45, 83] The A15 phase formed at w_{0_s} = 8.25 exhibits a unit cell parameter $a \approx$ 6.91 nm. The value of a of the A15 phase depends weakly on w_{0_s} and T in the range 22–100 °C: it monotonically increases from a = 6.81 nm to 6.92 nm with increasing w_{0_s} and it decreases by less than 3% (~ 0.2 nm) upon heating to 100 °C. In contrast to the LLCs formed at higher hydrations, the FK σ and A15 phases of **C$_{10}$Mal-TMA$_2$** remain thermally stable up to 100 °C. A temperature versus water content LLC phase diagram for **C$_{10}$Mal-TMA$_2$** is given in Figure 2B. Although windows of two-phase coexistence are anticipated at intermediate compositions and temperatures between each pure LLC phase window according to Gibbs Phase Rule,[2, 86] our phase mapping methodology employed a resolution specified by the headgroup hydration increment $\Delta w_{0_s} = 1$–1.5 and temperature increment $\Delta T = 20$ °C. Thus, the absence of some of these expected two-phase windows in this phase map suggests that they are sufficiently narrow that we did not directly observe them in the investigated LLC compositions unless noted. Note that a high level of surfactant crystallinity when $w_{0_s} < 4$ prevents formation of homogeneous ordered phases and we instead observe coexistence of crystalline surfactant with a LLC phase. Thus, we do not observe the hexagonally-packed cylinders (H_I) LLCs that arise from minimal hydration of the previously reported dianionic surfactant **DPA-TMA$_2$**.[72]

Decreasing the alkyl chain length of the malonate surfactant significantly impacts the observed LLC phase behavior, as assessed by SWAXS characterization of the water concentration-dependent mesophase morphologies of **C$_8$Mal-TMA$_2$** (Figure 3). The lyotropic order-disorder transition hydration below which ordered LLC phases form considerably decreases from $w_{0_s,\mathrm{ODT}} = 40$ for **C$_{10}$Mal-TMA$_2$** to $w_{0_s,\mathrm{ODT}} = 18$ in **C$_8$Mal-TMA$_2$**. In proximity to this ordering transition at $w_{0_s} = 16$–18, we observe phase coexistence of an ordered BCC LLC with a fluid isotropic dispersion of micelles as evidenced by the broadened base of the primary SWAXS peak (Figure 3A). Notably, the HCP spheres phase of the **C$_{10}$Mal-TMA$_2$** does not form in this shorter tail malonate amphiphile analog. We observe the formation of FK σ phases upon further reduction of the LLC water content to $11 \leq w_{0_s} \leq 16$, with weakly w_{0_s}-dependent unit cell parameters $a = 11.4$ nm and $c = 5.99$ nm ($c/a = 0.525$) (see Figure S2 for fully indexed pattern and Table S2 for a complete listing of peak positions and residuals). Given that the micelles of **C$_8$Mal-TMA$_2$** are expected to be smaller than those of the C_{10} analog, the unit cell parameters for this σ phase are noted to be ~ 15% smaller. We also find that reducing the surfactant tail length from C_{10} to C_8 renders the lattice order-disorder transition temperatures for FK σ phases accessible with $T_{\mathrm{ODT}} \leq 70$ °C, and T_{ODT} decreases monotonically with increasing w_{0_s}. Finally, A15 phases formed from samples with $w_{0_s} = 4$–8.25 display cubic unit cell parameters $a = 5.82$ nm and accessible T_{ODT}'s ≤ 90 °C (see Figure S3 for fully indexed pattern). Figure 3B depicts a temperature versus composition phase diagram for **C$_8$Mal-TMA$_2$** LLCs; again, not all of the expected two-phase coexistence windows[2] were observed given the headgroup hydration increment resolution of our phase map Δw_{0_s} = 1–1.5 and the temperature increment ΔT = 20 °C. Inspection of these data reveals that LLCs based on the C_{10} surfactant display higher T_{ODT}'s than those of the C_8 homolog at comparable values of w_{0_s}.

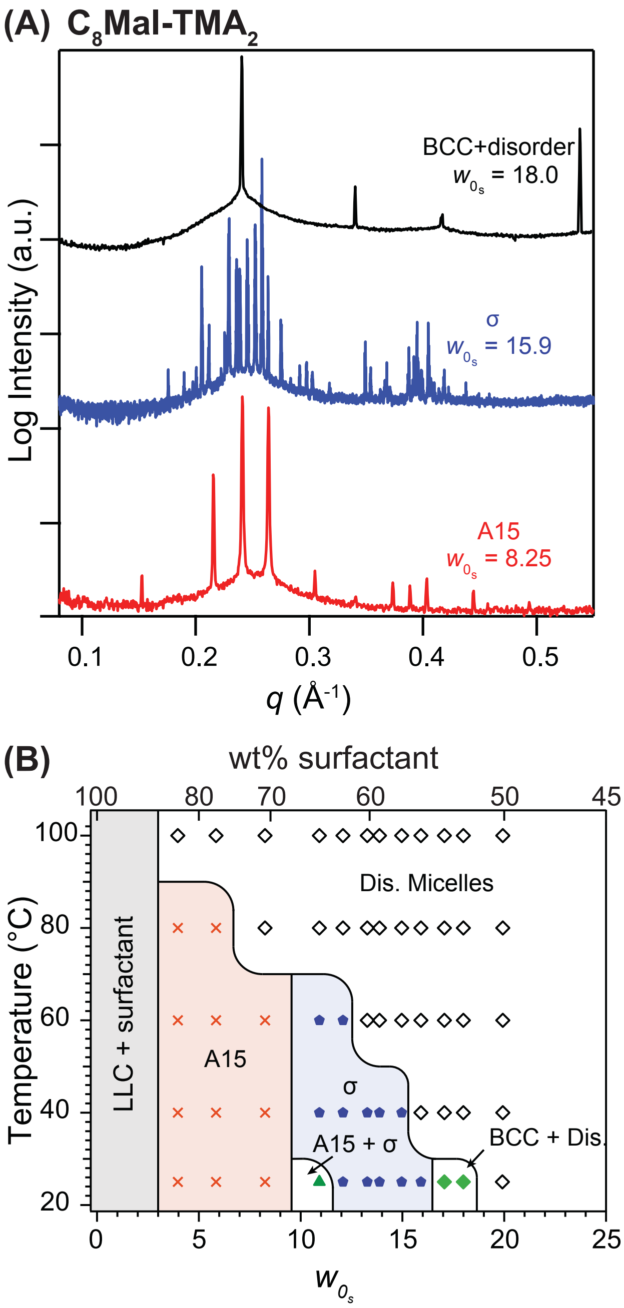

Figure 3. (A) Synchrotron SWAXS powder patterns for aqueous LLCs derived from **C_8Mal-TMA$_2$**, illustrating the formation of A15 and σ ordered phases, and coexistence of BCC and disordered micelles at 25 °C. (B) Temperature versus surfactant hydration number w_{0_s} phase diagram showing the lyotropic phase progression: disordered micelles → BCC + disordered micelles → σ → A15 with decreasing w_{0_s}.

Changing the identity of the counterion in **C_8Mal-TMA$_2$** from TMA$^+$ to K$^+$, as in **C_8Mal-K$_2$**, dramatically alters the observed LLC phase behavior (Figure 4). First, we observe an increase in the

$w_{0_s,\mathrm{ODT}} = 23$ for the potassium-containing LLCs. We also find no evidence for a BCC phase proximal to the lyotropic order-disorder transition hydration $w_{0_s,\mathrm{ODT}}$, within the resolution of our LLC phase map. The presence of the alkali counterion also eliminates the σ mesophase window, in favor of an enlarged A15 phase that forms when w_{0_s} = 9–22 with no accessible T_{ODT} (> 100 °C) by SWAXS analyses (Figure 4A). The lattice parameters for the A15 LLCs decrease monotonically from a = 6.28 nm to 5.99 nm upon increasing w_{0_s}. This unit cell shrinkage with increasing w_{0_s} is quite different from the monotonic increase of the A15 and σ phase unit cell dimensions for the TMA$^+$-based surfactants. Also noteworthy is the fact that the A15 unit cells of **C$_8$Mal-K$_2$** are generally larger than those of **C$_8$Mal-TMA$_2$** at comparable w_{0_s} values. For example, a = 6.28 nm at w_{0_s} = 9.84 for **C$_8$Mal-K$_2$**, whereas a = 5.82 nm when w_{0_s} = 8.25 for **C$_8$Mal-TMA$_2$**. Finally, we found that the A15 phase gives way to a thermally stable H$_{\mathrm{I}}$ phase at low hydrations w_{0_s} = 5–7 in **C$_8$Mal-K$_2$**, with a narrow intervening window of H$_{\mathrm{I}}$/A15 two-phase coexistence (Figure 4A and 4B). Within the headgroup hydration and temperature resolution increments of our experiment, we observe no other two-phase coexistence windows. SWAXS patterns for the latter coexisting phases appear as direct superpositions of the adjacent pure phase LLC. Based on these counterion-dependent differences in the LLC phase behaviors of the C$_8$– and C$_{10}$–alkylmalonate surfactants, we hypothesized that the highly dissociated nature of the soft, polarizable, and slightly hydrophobic TMA$^+$ counterion was essential for LLC FK σ phase formation.

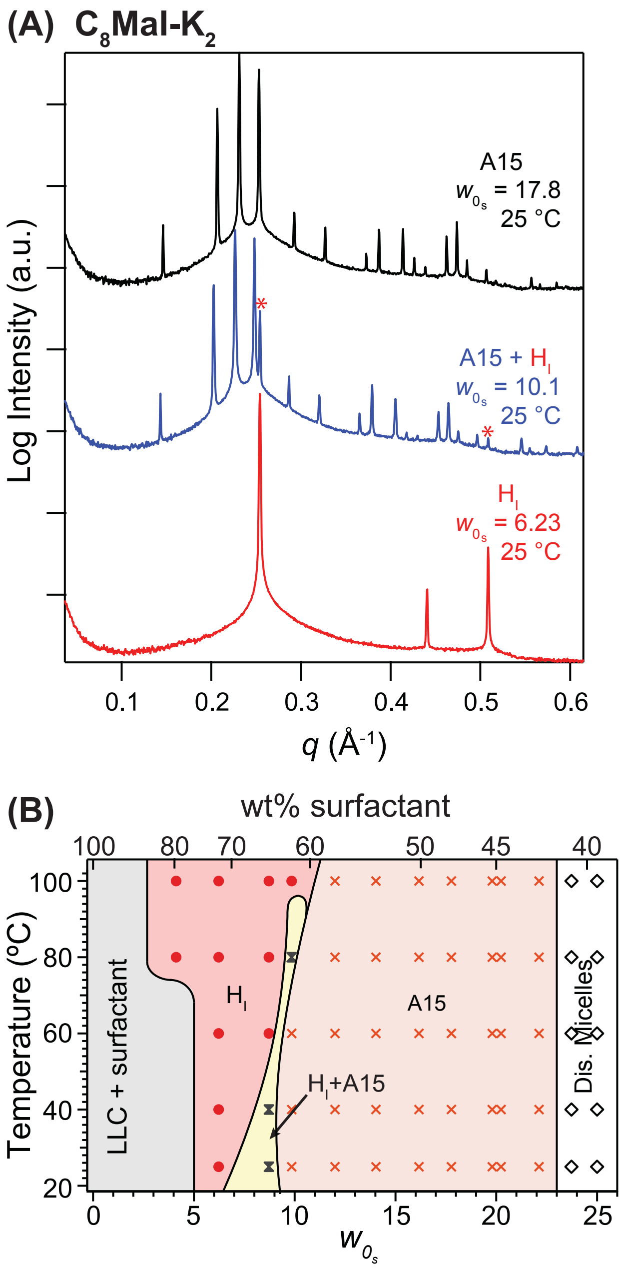

Figure 4. (A) Synchrotron SWAXS powder patterns for **C$_8$Mal-K$_2$** LLCs illustrating the formation of hexagonally–packed cylinders (H$_I$), H$_I$/A15 two-phase coexistence (* demarcates peaks corresponding to the H$_I$ phase), and pure A15 sphere packing phases. (B) Temperature versus w_{0_s} phase diagram, which notably lacks a FK σ phase.

In order to test this last hypothesis regarding the role of counterion identity in LLC phase selection, we examined the phase behaviors of alkylmalonate surfactants bearing polarizable and slightly hydrophobic Cs$^+$ counterions. We synthesized samples of **C$_n$Mal-Cs$_2$** (n = 8 and 10) by deprotonation of the parent malonic acids with Cs$_2$CO$_3$. Figure 5A summarizes the aqueous LLC phase behavior of **C$_8$Mal-Cs$_2$**, which displays hybrid behavior between that of amphiphiles with either TMA$^+$ or K$^+$

counterions (see Figure S4A for representative 1D SWAXS intensity profiles on which these phase diagrams are based). We explicitly found that the $w_{0_s,\mathrm{ODT}} \approx 26$ is somewhat higher for **C_8Mal-Cs_2** than that for **C_8Mal-K_2** and that the Cs-surfactant forms a modestly stable BCC LLC near this lyotropic ODT with $T_{ODT} < 60$ °C. In the hydration range $w_{0_s} = 8–24.5$, as-formed LLCs exhibit A15 morphologies that are thermally stable up to $T > 100$ °C with one notable exception. At $w_{0_s} = 22.8$, the LLC obtained from iterative cycles of high-speed centrifugation and hand-mixing exhibits A15/σ two-phase coexistence (Figure S4A). Upon heating this sample to 40 °C, we observe a thermally-induced transition to a pure A15 phase that remains stable up to 100 °C. Since cooling this specific LLC composition back to 22 °C does not recover the coexisting phases, we suggest that the complex σ phase is metastable with respect to the A15 structure in **C_8Mal-Cs_2** LLCs. SWAXS reveals that the A15 unit cell parameter for **C_8Mal-Cs_2** is $a \approx 6.17$ nm at $w_{0_s} = 8.00$, which is ~6% greater than that of a comparably hydrated **C_8Mal-TMA_2** A15 LLC. The unit cell parameters for **C_8Mal-Cs**$_2$ are comparable to **C_8Mal-K_2**, and they show only weak temperature dependence as with the other counterions. The unit cell parameter also decreases with increasing w_{0_s}, similar to **C_8Mal-K_2,** although the dependence on headgroup hydration is much weaker. As with the potassium-based surfactants, **C_8Mal-Cs_2** forms a H_I morphology at headgroup hydrations lower than that of the A15 phase. In the case of **C_{10}Mal-Cs_2**, we observe a similar water concentration-dependent phase progression BCC + Iso → HCP → A15/σ → A15 → H_I/A15 → H_I with decreasing w_{0_s} at ambient temperature (Figure 5B). Although Gibbs Phase Rule again anticipates a pure σ phase and a σ/HCP (or σ/BCC) two-phase coexistence window at high hydrations of **C_{10}Mal-Cs_2**, the limited resolution of our phase map ($\Delta w_{0_s} = 1\text{-}2$ and $\Delta T = 20$ °C) did not permit their observation. Representative SWAXS data for **C_{10}Mal–Cs_2** are given in Figure S4B. We note that most of these phases are thermally stable, with the exception of the HCP LLC that exhibits a thermoreversible transition to a BCC phase at $T \geq 80$ °C. Notably, lengthening the surfactant tail stabilizes the coexisting

A15 and σ phases and does not lead to the apparent σ phase metastability observed in the corresponding C_8 surfactant.

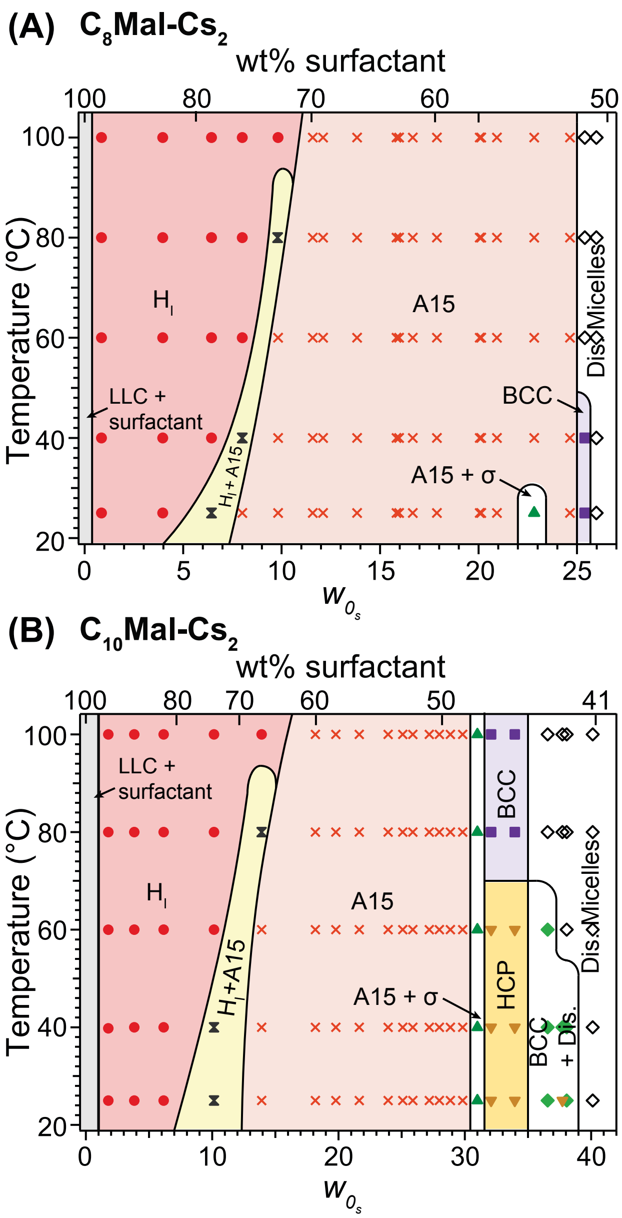

Figure 5. Temperature versus surfactant hydration number w_{0_s} phase diagram for aqueous LLCs of (A) **C_8Mal-Cs$_2$** and (B) **C_{10}Mal-Cs$_2$**, which shows that the soft and somewhat hydrophobic Cs$^+$ counterions allow σ phase formation in narrow composition windows.

Discussion

Kim *et al*. rationalized the **DPA-TMA$_2$** lyotropic phase sequence BCC → σ → A15 → H_I with decreasing w_{0_s} in terms of a frustrated force balance within these supramolecular assemblies.[72]

Molecular dynamics (MD) simulations revealed that the water–solvated TMA$^+$ counterions in the aqueous domains of these LLCs mediate electrostatic cohesion between the quasispherical alkylphosphonate (anionic) micelles. The lowest free energy counterion configuration in these ordered LLCs localizes them near the midplanes bisecting line segments, which connect the centers of neighboring micelles. Geometrically, the counterions are thus concentrated along the polyhedral interfaces of the Voronoi (or Wigner-Seitz) cells associated with each site in the ordered lattice. Electrostatic correlations between the counterions and the surfactant headgroups consequently drive soft faceting of the micelles. However, the formation of a polyhedral counterion cloud around each facetted micelle is unfavorable, since the ions and surfactant headgroups situated at the edges and vertices of the polyhedra are differentially hydrated as compared to those sitting on the faces. Each micelle instead tends toward ionic sphericity, that is, formation of a spherically symmetric particle (with constant mean curvature) wherein the counterions are isotropically distributed around the core. At a given w_{0_s}, the LLC assembly must optimize intermicellar cohesion while also maximizing the average ionic sphericity of its constituent micelles. As the micelles become more concentrated within a BCC LLC (decreasing w_{0_s}), the counterion clouds deviate significantly from the preferred ionic sphericity due to decreased nearest neighbor distances in the ordered lattice. Beyond a critical reduction in w_{0_s}, the LLC reconfigures by interparticle chain exchange of surfactants and their counterions to generate a new configuration that optimizes both ionic sphericity and ensemble electrostatic cohesion. The lattice sites in the new LLC morphology have a greater number of nearest neighbors (average coordination numbers $CN > 12$) to induce greater faceting of the counterion clouds to render them more spherical. However, the higher average lattice site CN results in a lower overall lattice symmetry. Furthermore, the micelles in this new phase are not all of the same size or volume: adoption of a lower packing symmetry induces the formation of a discrete distribution of particle sizes with discrete aggregation numbers.

The sphericity of a polyhedron may be quantified through the isoperimetric quotient, $IQ = 36\pi S^3/V^2$ such that $IQ = 1$ for a perfect sphere.[38] On this basis, the number average IQ calculated from the constituent Voronoi cell *IQ*s in an ordered lattice quantifies the overall sphericity of that packing symmetry. On this basis, one calculates that *IQ*(σ) > *IQ*(A15) > *IQ*(BCC) > *IQ*(HCP).[73, 74] Thus, the balance of ionic sphericity and interparticle cohesion leads **DPA-TMA$_2$** micelles to form FK σ phases across the range w_{0_s} = 21–31 and A15 phases when w_{0_s} = 10–18. We note that the initial formation of BCC just below $w_{0_s,\mathrm{ODT}}$ = 44 probably arises for entropic reasons[84] in spite of the obvious deviation from maximal sphericity.

While the ionic sphericity concept should apply to all aqueous lyotropic packings of ionic spherical micelles, our studies reveal that access to the FK σ phase depends on the nature of the surfactant headgroup. We first note that the phase diagrams given in Figure 2B and 3B establish that single-tail dianionic surfactants bearing TMA$^+$ counterions generally appear to self-assemble into FK σ phase LLCs. However, **C$_{10}$Mal-TMA$_2$** surfactants display a relatively smaller FK σ phase window width (Δw_{0_s} = 4) as compared to **DPA-TMA$_2$** (Δw_{0_s} = 10), in spite of their both having C$_{10}$-alkyl tails. In aqueous **C$_{10}$Mal-TMA$_2$** LLCs at 22 °C, the phase sequence HCP → σ → A15 with a relatively small σ phase window suggests that this surfactant does not enforce ionic sphericity as strictly as **DPA-TMA$_2$**. In other words, the alkylmalonate-derived micelles are softer and more deformable than the alkylphosphonate micelles. Thus, greater deviations from ionic sphericity are allowed in the former case. The origins of this enhanced particle deformability probably lie in the relative strengths of the counterion-headgroup correlations, which are directly related to the surfactant headgroup chemistries. **DPA-TMA$_2$** forms high curvature micelles that are relatively rigid due to strong Coulombic repulsions between adjacent dianionic headgroups situated at the water/hydrophobic interface, with only partial screening by the highly dissociated TMA$^+$ counterions. While the malonate headgroup of **C$_{10}$Mal-TMA$_2$** is nominally dianionic, the close spatial proximity of the two anionic carboxylate headgroups linked through a one carbon bridge leads the counterions to sit closer to the micelle surface to screen both intramolecular and inter-headgroup electrostatic repulsions. The lower degree of counterion dissociation leads the decylmalonate surfactant to form larger micelles with interfaces that are more deformable. Enhanced micelle deformability probably also enables formation of the lower sphericity HCP packing at high hydrations and low temperatures near $w_{0_s,\mathrm{ODT}}$.

Naturally, the question arises as to why the σ phase window width Δw_{0_s} for **C$_{10}$Mal-TMA$_2$** is smaller than that for **C$_8$Mal-TMA$_2$**. Alkylmalonates with shorter *n*-alkyl tails form micelles with smaller radii, with more tightly packed anionic headgroups lining their surfaces. The enhanced electrostatic repulsions amongst these ionic headgroups and the short alkyl tail length likely rigidifies these spherical particles, leading to a stronger preference for ionic sphericity. The larger C_{10} micelles have a decreased surface area-to-volume ratio leading to a smaller effective headgroup area per surfactant. Thus, the counterions are more closely associated with the micelle surface[87] and the more deformable interface enables formation of lower sphericity morphologies.

Upon changing the surfactant counterion from TMA^+ to K^+ with **C$_8$Mal**, we observe that the σ phase window closes at the expense of widening that of the A15 morphology. The inaccessibility of the σ phase in K-based surfactant LLCs likely reflects a higher degree of potassium carboxylate association,[88] which enables formation of larger and more deformable micelles that pack into lower sphericity LLCs by the above mechanism. Note that the intermediate level of Cs^+– carboxylate association[17] in **C$_8$Mal-Cs$_2$** allows the formation of a metastable σ phase at low temperatures, which irreversibly converts to an aqueous A15 LLC. This behavior probably reflects subtle differences in alkali-carboxylate ion pair dissociation that are only discernable by virtue of the cooperative nature of lyotropic self-assembly, in which the morphology serves as a macroscopic reporter for microscopic interactions.

We can also explain the expansion of the A15 unit cell parameters upon exchanging the TMA^+ counterions for K^+ in the **C$_8$Mal** LLCs, by considering the specific counterion distributions between the micelles in the aqueous domains. Recall that the counterions in each LLC sphere packing localize along the Voronoi cell boundaries of each lattice site, in order to maximize interparticle cohesion. The breadth of the counterion distribution along these Voronoi boundaries depends on the relative strengths of their pairwise electrostatic repulsions. Soft and polarizable TMA^+ cations, in which the positive charge is delocalized across the four methyl groups, can more densely concentrate along the Voronoi cell boundaries as compared to the more point-like K^+ ions that are correlated over much larger distances.[89] To experimentally support this notion, we used our established methodology to reconstruct the electron density maps for A15 LLCs based on **C_8Mal-K_2** and **C_8Mal-TMA_2** at w_{0_s} = 9.85 and w_{0_s} = 8.25, respectively (Figure 6A; see Supporting Information for electron density map reconstruction details). Figure 6B depict the normalized electron density variation in the $z = 0$ plane along vectors parallel to the [010] direction connecting the centers of the platelet micelles (*6f* Wyckoff positions) and to the [100] direction along the unit cell edge, as a function of the dimensionless fractional lattice parameter for A15 phases with K^+ and TMA^+ counterions. The electron density was normalized by the linear density along this vector (area under the raw linear plot), wherein we arbitrarily assigned the highest density regions to be the cores of the micelles. We specifically use the dimensionless fractional distance to compare these two phases at slightly different hydrations, since they have different unit cell parameters. By our convention, the maxima in this plot correspond to the micelle cores and the broad minimum stems from the counterion distributions between the surfaces of neighboring micelles. Qualitative inspection of the plots in Figure 6B reveal that the trough for the TMA^+ counterions is narrower and deeper than that for the K^+ ions, indicating denser localization of TMA^+ along the Voronoi cell boundaries as expected. On the other hand, the shallower and broader troughs corresponding to the K^+ counterions in the aqueous nanodomains implies their more diffuse counterion clouds. The counterion distributions deduced from the experimental SWAXS data are consistent with the notion that the K^+ ions are more closely associated with the carboxylate headgroups than the TMA^+ ions in these **C_8Mal** A15 LLCs at comparable hydrations. Consequently, the unit cell dimensions are larger for the surfactant LLCs with K^+ counterions due to electrostatic repulsions between the correlated, point-like charges in a manner consistent with expectations based on theory by Jho *et al.*[90]

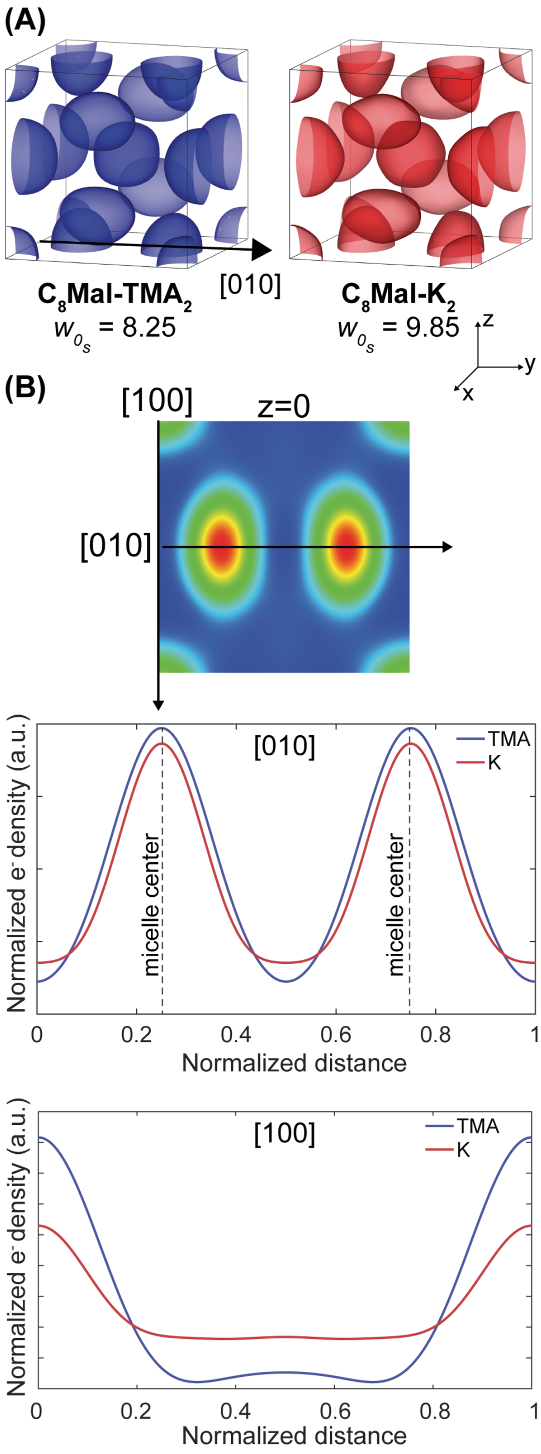

Figure 6. (A) 90% isosurface electron density reconstructions of the A15 phase unit cells for **C$_8$Mal-TMA$_2$** and **C$_8$Mal-K$_2$** at w_{0_s} = 8.25 and 9.85 respectively. (B) Normalized linear electron density profile in the $z = 0$ plane along the [010] direction passing through the centers of the platelet micelles and in the [100] direction along the unit cell edge. The peaks correspond to the micelle cores and the troughs correspond to the counterion distribution between neighboring micelles. The relative depth and breadths of the troughs in both of the [010] and [100] directions indicate that the counterions are more localized along the Voronoi cell boundaries in the case of TMA$^+$ (*blue*) than with K$^+$ (*red*).

Finally, we note that the values of $w_{0_s,\mathrm{ODT}}$ is generally higher for surfactants with alkali counterions as opposed to those with TMA$^+$ counterions. Since the alkali counterions are electrostatically correlated over longer distances by virtue of their point-like charge distributions,[89] we surmise that larger amounts of water are required in order to effectively screen all of the pairwise interactions between the micelles and induce lattice disordering. However, the more diffuse and polarizable nature of the TMA$^+$ counterion lends to its effective screening by smaller amounts of water. Therefore, cohesion between the micelles is lost at relatively lower hydrations for the TMA-based surfactants.

Conclusions

Detailed studies of the water concentration–dependent lyotropic mesophase behaviors of a homologous series of 2-alkylmalonate ionic surfactants revealed their propensities to form four possible spherical micelle packings, the exact symmetries of which depend sensitively on their associated counterions. The soft, polarizable TMA$^+$ ion leads to the formation of micelles that strongly prefer a local spherical particle symmetry, since the high degree of counterion-headgroup dissociation fosters significant electrostatic repulsions between adjacent surfactant headgroups within each micelle. This preference for ionic sphericity while maximizing micellar cohesion drives a spontaneous lowering of the global lattice symmetry to form a complex FK σ phase, the unit cell of which contains 30 quasispherical particles with five different volumes. Reducing the water content of these LLCs drives formation of the structurally related FK A15 phase. However, replacing the soft TMA$^+$ counterion with a more point-like K$^+$ counterion completely destabilizes the σ phase in favor of the A15 phase. This change in packing symmetry originates from the reduced preference for spherical particle symmetry, which arises from closer counterion-headgroup association in the latter case. These findings generally suggest that controlling both counterion-headgroup and counterion-counterion correlations in normal LLC phases furnish new means for self-assembling hydrated surfactants into unusual mesostructured supramolecular assemblies with tunable unit cell sizes.

ASSOCIATED CONTENT

Supporting Information

The Supporting Information is available free of charge on the ACS Publications website at DOI: 10.1021/acs.langmuir.xxxxxxx.

Fully indexed σ and A15 patterns, 1D SWAXS patterns for $\mathbf{C_nMal\text{-}Cs_2}$, electron density reconstructions for the σ phase formed by $\mathbf{C_8Mal\text{-}TMA_2}$ and $\mathbf{C_{10}Mal\text{-}TMA_2}$**.** (Figures S1-S5, Tables S1 and S2).

Description of the electron density map reconstruction methodology for the A15 phases for $\mathbf{C_8Mal\text{-}TMA_2}$ and $\mathbf{C_8Mal\text{-}K_2}$ (w_{0_s} = 8.25, 9.85 respectively), and σ phases for $\mathbf{C_8Mal\text{-}TMA_2}$ and $\mathbf{C_{10}Mal\text{-}TMA_2}$ (w_{0_s} = 15.91, 22.21 respectively). (PDF)

AUTHOR INFORMATION

Author Contributions

This manuscript was written through contributions of all authors, and all authors have given approval to the final version of the manuscript.

Notes

The authors declare no competing financial interest.

Acknowledgment

This work has supported by National Science Foundation grant CHE-1608115. Synchrotron SAXS analyses were conducted at Sector 12 of the Advanced Photon Source (APS), a U.S. Department of Energy (DOE) Office of Science User Facility operated for the DOE Office of Science by Argonne National Laboratory under Contract No. DE-AC02-06CH11357. Research reported in this publication was supported by the Office of the Director, National Institutes of Health of the National Institutes of

Health under Award Number S10OD011952. The content is solely the responsibility of the authors and does not necessarily represent the official views of the National Institutes of Health. We also thank Dr. Sung Kim, Dr. Tyler J. Mann and Grayson L. Jackson for helpful discussions.

References

1. Chandler, D. Interfaces and the Driving Force of Hydrophobic Assembly. *Nature* **2005,** *437*, 640-647.

2. Laughlin, R. G., *The Aqueous Phase Behavior of Surfactants*. Academic Press, London: 1996.

3. Dreiss, C. A. Wormlike Micelles: Where Do We Stand? Recent Developments, Linear Rheology and Scattering Techniques. *Soft Matter* **2007,** *3*, 956-970.

4. Raghavan, S. R.; Feng, Y., Wormlike Micelles: Solutions, Gels, or Both? in *Wormlike Micelles*, Dreiss, C. A.; Feng, Y., Eds. Royal Society of Chemistry: 2017; pp 9-30.

5. Walker, L. M. Rheology and Structure of Worm-Like Micelles. *Curr. Opin. Colloid Interface Sci.* **2001,** *6*, 451-456.

6. Kim, H.; Leal, C. Cuboplexes: Topologically Active siRNA Delivery. *ACS Nano* **2015,** *9*, 10214-10226.

7. Leal, C.; Bouxsein, N. F.; Ewert, K. K.; Safinya, C. R. Highly Efficient Gene Silencing Activity of siRNA Embedded in a Nanostructured Gyroid Cubic Lipid Matrix. *J. Am. Chem. Soc.* **2010,** *132*, 16841-16847.

8. Mulet, X.; Boyd, B. J.; Drummond, C. J. Advances in Drug Delivery and Medical Imaging Using Colloidal Lyotropic Liquid Crystalline Dispersions. *J. Colloid Interface Sci.* **2013,** *393*, 1-20.

9. Negrini, R.; Mezzenga, R. Diffusion, Molecular Separation, and Drug Delivery from Lipid Mesophases with Tunable Water Channels. *Langmuir* **2012,** *28*, 16455-16462.

10. Israelachvili, J. N.; Mitchell, D. J.; Ninham, B. W. Theory of Self-Assembly of Lipid Bilayers and Vesicles. *Biochim. Biophys. Acta* **1977,** *470*, 185-201.

11. Tanford, C. Micelle Shape and Size. *J. Phys. Chem.* **1972,** *76*, 3020-3024.

12. Tanford, C., *The Hydrophobic Effect: Formation of Micelles and Biological Membranes*. 2nd ed.; John Wiley & Sons Limited: Sussex, England, 1980.

13. Israelachvili, J. N., *Intermolecular and Surface Forces*. 3rd ed.; Academic Press: London, 2011.

14. Nagarajan, R., One Hundred Years of Micelles: Evolution of the Theory of Micellization in *Surfactant Science and Technology*, Romsted, L. S., Ed. CRC Press: Boca Raton, 2014; pp 3–53.

15. Nagarajan, R. Molecular Packing Parameter and Surfactant Self-Assembly: The Neglected Role of the Surfactant Tail. *Langmuir* **2002,** *18*, 31-38.

16. Hagslaett, H.; Soederman, O.; Joensson, B. Divalent Surfactants. Experimental Results and Theoretical Modeling of Surfactant/Water Phase Equilibria. *Langmuir* **1994,** *10*, 2177-2187.

17. Vlachy, N.; Drechsler, M.; Verbavatz, J.-M.; Touraud, D.; Kunz, W. Role of the Surfactant Headgroup on the Counterion Specificity in the Micelle-to-Vesicle Transition through Salt Addition. *J. Colloid Interface Sci.* **2008,** *319*, 542-548.

18. Mondal, J.; Mahanthappa, M.; Yethiraj, A. Self-Assembly of Gemini Surfactants: A Computer Simulation Study. *J. Phys. Chem. B* **2013,** *117*, 4254-4262.

19. Berg, J. C., *An Introduction to Interfaces & Colloids: The Bridge to Nanoscience*. World Scientific: Hackensack, NJ, 2010.

20. Hiemenz, P. C.; Rajagopalan, R., *Principles of Colloid and Surface Chemistry*. 3rd ed.; Marcel Dekker, Inc.: New York, 1997.

21. Mezzenga, R., Physics of Self-Assembly of Lyotropic Liquid Crystals in *Self-Assembled Supramolecular Architectures: Lyotropic Liquid Crystals*, Garti, N.; Somasundaran, P.; Mezzenga, R., Eds. John Wiley & Sons, Inc.: Hoboken, NJ, 2012; pp 1-20.

22. Kato, T.; Mizoshita, N.; Kishimoto, K. Functional Liquid-Crystalline Assemblies: Self-Organized Soft Materials. *Angew. Chem. Int. Ed.* **2005,** *45*, 38-68.

23. Seddon, J. M. Structure of the Inverted Hexagonal (H_{II}) Phase, and Non-Lamellar Phase Transitions of Lipids. *Biochim. Biophys. Acta* **1990,** *1031*, 1-69.

24. Hyde, S. T., Chapter 16: Identification of Lyotropic Liquid Crystalline Mesophases in *Handbook of Applied Surface and Colloid Chemistry*, Holmberg, K., Ed. John Wiley & Sons, Ltd.: New York, 2001; Vol. 2, pp 299-332.

25. Seddon, J. M.; Templer, R. H.; Lipowsky, R.; Sackmann, E., Chapter 3: Polymorphism of Lipid-Water Systems in *Handbook of Biological Physics*, North Holland (Elsevier): New York, 1995; Vol. Volume 1, Part 1, pp 97-160.

26. Werber, J. R.; Osuji, C. O.; Elimelech, M. Materials for Next-Generation Desalination and Water Purification Membranes. *Nature Rev. Mater.* **2016,** *1*, 16018/1–16018/15.

27. Zhou, M.; Nemade, P. R.; Lu, X.; Zeng, X.; Hatakeyama, E. S.; Noble, R. D.; Gin, D. L. New Type of Membrane Material for Water Desalination Based on a Cross-Linked Bicontinuous Cubic Lyotropic Liquid Crystal Assembly. *J. Am. Chem. Soc.* **2007,** *129*, 9574-9575.

28. Kerr, R. L.; Miller, S. A.; Shoemaker, R. K.; Elliott, B. J.; Gin, D. L. New Type of Li Ion Conductor with 3D Interconnected Nanopores Via Polymerization of a Liquid Organic Electrolyte-Filled Lyotropic Liquid-Crystal Assembly. *J. Am. Chem. Soc.* **2009,** *131*, 15972-15973.

29. Jackson, G. L.; Perroni, D. V.; Mahanthappa, M. K. Roles of Chemical Functionality and Pore Curvature in the Design of Nanoporous Proton Conductors. *J. Phys. Chem. B* **2017,** *121*, 9429-9436.

30. Clapper, J. D.; Sievens-Figueroa, L.; Guymon, C. A. Photopolymerization in Polymer Templating. *Chem. Mater.* **2007,** *20*, 768-781.

31. Davis, M. E. Ordered Porous Materials for Emerging Applications. *Nature* **2002,** *417*, 813-821.

32. Han, L.; Che, S. Anionic Surfactant Templated Mesoporous Silicas (AMSs). *Chem. Soc. Rev.* **2013,** *42*, 3740-3752.

33. Wan, Y.; Zhao, D. On the Controllable Soft-Templating Approach to Mesoporous Silicates. *Chem. Rev.* **2007,** *107*, 2821-2860.

34. Yaghmur, A.; Glatter, O. Characterization and Potential Applications of Nanostructured Aqueous Dispersions. *Adv. Colloid Interface Sci.* **2009,** *147*, 333-342.

35. Shearman, G. C.; Tyler, A. I. I.; Brooks, N. J.; Templer, R. H.; Ces, O.; Law, R. V.; Seddon, J. M. Ordered Micellar and Inverse Micellar Lyotropic Phases. *Liq. Cryst.* **2010,** *37*, 679-694.

36. De Graef, M.; McHenry, M. E., *Structure of Materials: An Introduction to Crystallography, Diffraction and Symmetry*. Cambridge University Press: 2012.

37. Ziherl, P.; Kamien, R. D. Soap Froths and Crystal Structures. *Phys. Rev. Lett.* **2000,** *85*, 3528-3531.

38. Grason, G. M. The Packing of Soft Materials: Molecular Asymmetry, Geometric Frustration and Optimal Lattices in Block Copolymer Melts. *Phys. Rep.* **2006,** *433*, 1-64.

39. Balmbra, R. R.; Clunie, J. S.; Goodman, J. F. Cubic Mesomorphic Phases. *Nature* **1969,** *222*, 1159-1160.

40. Vargas, R.; Mariani, P.; Gulik, A.; Luzzati, V. Cubic Phases of Lipid-Containing Systems. *J. Mol. Bio.* **1992,** *225*, 137-145.

41. Luzzati, V.; Vargas, R.; Gulik, A.; Mariani, P.; Seddon, J. M.; Rivas, E. Lipid Polymorphism: A Correction. The Structure of the Cubic Phase of Extinction Symbol Fd-- Consists of Two Types of Disjointed Reverse Micelles Embedded in a Three-Dimensional Hydrocarbon Matrix. *Biochemistry* **1992,** *31*, 279-285.

42. Seddon, J. M.; Robins, J.; Gulik-Krzywicki, T.; Delacroix, H. Inverse Micellar Phases of Phospholipids and Glycolipids. *Phys. Chem. Chem. Phys.* **2000,** *2*, 4485-4493.

43. Martiel, I.; Sagalowicz, L.; Mezzenga, R. A Reverse Micellar Mesophase of Face-Centered Cubic Fm3(–)m Symmetry in Phosphatidylcholine/Water/Organic Solvent Ternary Systems. *Langmuir* **2013,** *29*, 15805-15812.

44. Shearman, G. C.; Tyler, A. I. I.; Brooks, N. J.; Templer, R. H.; Ces, O.; Law, R. V.; Seddon, J. M. A 3-D Hexagonal Inverse Micellar Lyotropic Phase. *J. Am. Chem. Soc.* **2009,** *131*, 1678-1679.

45. Perroni, D. V.; Mahanthappa, M. K. Inverse Pm3(-)n Cubic Micellar Lyotropic Phases from Zwitterionic Triazolium Gemini Surfactants. *Soft Matter* **2013,** *9*, 7919-7922.

46. Frank, F. C.; Kasper, J. S. Complex Alloy Structures Regarded as Sphere Packings. II. Analysis and Classification of Representative Structures. *Acta Crystallogr.* **1959,** *12*, 483-499.

47. Rivier, N. Kelvin's Conjecture on Minimal Froths and the Counter-Example of Weaire and Phelan. *Philos. Mag. Lett.* **1994,** *69*, 297-303.

48. Percec, V.; Mitchell, C. M.; Cho, W. D.; Uchida, S.; Glodde, M.; Ungar, G.; Zeng, X.; Liu, Y.; Balagurusamy, V. S.; Heiney, P. A. Designing Libraries of First Generation AB_3 and AB_2 Self-Assembling Dendrons Via the Primary Structure Generated from Combinations of $(AB)_{(Y)}$-AB_3 and $(AB)_{(Y)}$-AB_2 Building Blocks. *J. Am. Chem. Soc.* **2004,** *126*, 6078-6094.

49. Percec, V.; Peterca, M.; Tsuda, Y.; Rosen, B. M.; Uchida, S.; Imam, M. R.; Ungar, G.; Heiney, P. A. Elucidating the Structure of the Pm3(-)n Cubic Phase of Supramolecular Dendrimers through the Modification of Their Aliphatic to Aromatic Volume Ratio. *Chem. Eur. J.* **2009,** *15*, 8994-9004.

50. Ungar, G.; Liu, Y.; Zeng, X.; Percec, V.; Cho, W. D. Giant Supramolecular Liquid Crystal Lattice. *Science* **2003,** *299*, 1208-1211.

51. Huang, M.; Hsu, C. H.; Wang, J.; Mei, S.; Dong, X.; Li, Y.; Li, M.; Liu, H.; Zhang, W.; Aida, T.; Zhang, W. B.; Yue, K.; Cheng, S. Z. Selective Assemblies of Giant Tetrahedra Via Precisely Controlled Positional Interactions. *Science* **2015,** *348*, 424-428.

52. Liu, M.; Qiang, Y.; Li, W.; Qiu, F.; Shi, A.-C. Stabilizing the Frank-Kasper Phases Via Binary Blends of AB Diblock Copolymers. *ACS Macro Lett.* **2016,** *5*, 1167-1171.

53. Yue, K.; Huang, M.; Marson, R. L.; He, J.; Huang, J.; Zhou, Z.; Wang, J.; Liu, C.; Yan, X.; Wu, K.; Guo, Z.; Liu, H.; Zhang, W.; Ni, P.; Wesdemiotis, C.; Zhang, W.-B.; Glotzer, S. C.; Cheng, S. Z. D. Geometry Induced Sequence of Nanoscale Frank–Kasper and Quasicrystal Mesophases in Giant Surfactants. *Proc. Natl. Acad. Sci. U. S. A.* **2016,** *113*, 14195-14200.

54. Chanpuriya, S.; Kim, K.; Zhang, J.; Lee, S.; Arora, A.; Dorfman, K. D.; Delaney, K. T.; Fredrickson, G. H.; Bates, F. S. Cornucopia of Nanoscale Ordered Phases in Sphere-Forming Tetrablock Terpolymers. *ACS Nano* **2016,** *10*, 4961-4972.

55. Kim, K.; Schulze, M. W.; Arora, A.; Lewis, R. M.; Hillmyer, M. A.; Dorfman, K. D.; Bates, F. S. Thermal Processing of Diblock Copolymer Melts Mimics Metallurgy. *Science* **2017,** *356*, 520–523.

56. Lee, S.; Bluemle, M. J.; Bates, F. S. Discovery of a Frank-Kasper σ Phase in Sphere-Forming Block Copolymer Melts. *Science* **2010,** *330*, 349-353.

57. Schulze, M. W.; Lewis III, R. M.; Lettow, J. H.; Hickey, R. J.; Gillard, T. M.; Hillmyer, M. A.; Bates, F. S. Conformational Asymmetry and Quasicrystal Approximants in Linear Diblock Copolymers. *Phys. Rev. Lett.* **2017,** *118*, 207801/1–207801/5.

58. Balagurusamy, V.; Ungar, G.; Percec, V.; Johansson, G. Rational Design of the First Spherical Supramolecular Dendrimers Self-Organized in a Novel Thermotropic Cubic Liquid-Crystalline Phase and the Determination of Their Shape by X-Ray Analysis. *J. Am. Chem. Soc.* **1997,** *119*, 1539-1555.

59. Holerca, M. N.; Sahoo, D.; Peterca, M.; Partridge, B. E.; Heiney, P. A.; Percec, V. A Tetragonal Phase Self-Organized from Unimolecular Spheres Assembled from a Substituted Poly(2-Oxazoline). *Macromolecules* **2017,** *50*, 375-385.

60. Hudson, S. D.; Jung, H.-T.; Percec, V.; Cho, W.-D.; Johansson, G.; Ungar, G.; Balagurusamy, V. S. K. Direct Visualization of Individual Cylindrical and Spherical Supramolecular Dendrimers. *Science* **1997,** *278*, 449-452.

61. Percec, V.; Ahn, C. H.; Ungar, G.; Yeardley, D. J. P.; Möller, M.; Sheiko, S. S. Controlling Polymer Shape through the Self-Assembly of Dendritic Side-Groups. *Nature* **1998,** *391*, 161–164.

62. Rosen, B. M.; Wilson, C. J.; Wilson, D. A.; Peterca, M.; Imam, M. R.; Percec, V. Dendron-Mediated Self-Assembly, Disassembly, and Self-Organization of Complex Systems. *Chem. Rev.* **2009,** *109*, 6275-6540.

63. Rosen, B. M.; Wilson, D. A.; Wilson, C. J.; Peterca, M.; Won, B. C.; Huang, C.; Lipski, L. R.; Zeng, X.; Ungar, G.; Heiney, P. A.; Percec, V. Predicting the Structure of Supramolecular Dendrimers via the Analysis of Libraries of AB_3 and Constitutional Isomeric AB_2 Biphenylpropyl Ether Self-Assembling Dendrons. *J. Am. Chem. Soc.* **2009,** *131*, 17500-17521.

64. Yeardley, D. J. P.; Ungar, G.; Percec, V.; Holerca, M. N.; Johansson, G. Spherical Supramolecular Minidendrimers Self-Organized in an "Inverse Micellar"-Like Thermotropic Body-Centered Cubic Liquid Crystalline Phase. *J. Am. Chem. Soc.* **2000,** *122*, 1684-1689.

65. Janot, C., *Quasicrystals—a Primer (Monographs on the Physics and Chemistry of Materials)*. Oxford University Press: Oxford, 1994.

66. Steurer, W.; Deloudi, S., *Crystallography of Quasicrystals: Concepts, Methods, and Structures*. Springer-Verlag: Berlin, 2009; Vol. 126.

67. Shechtman, D.; Blech, I.; Gratias, D.; Cahn, J. W. Metallic Phase with Long-Range Orientational Order and No Translational Symmetry. *Phys. Rev. Lett.* **1984,** *53*, 1951–1953.

68. Zeng, X.; Ungar, G.; Liu, Y.; Percec, V.; Dulcey, A. E.; Hobbs, J. K. Supramolecular Dendritic Liquid Quasicrystals. *Nature* **2004,** *428*, 157-160.

69. Gillard, T. M.; Lee, S.; Bates, F. S. Dodecagonal Quasicrystalline Order in a Diblock Copolymer Melt. *Proc. Natl. Acad. Sci. U. S. A.* **2016,** *113*, 5167-5172.

70. Zhang, J.; Bates, F. S. Dodecagonal Quasicrystalline Morphology in a Poly (styrene-*b*-isoprene-*b*-styrene-*b*-ethylene oxide) Tetrablock Terpolymer. *J. Am. Chem. Soc.* **2012,** *134*, 7636-7639.

71. Fischer, S.; Exner, A.; Zielske, K.; Perlich, J.; Deloudi, S.; Steurer, W.; Lindner, P.; Förster, S. Colloidal Quasicrystals with 12-Fold and 18-Fold Diffraction Symmetry. *Proc. Natl. Acad. Sci. U. S. A.* **2011,** *108*, 1810-1814.

72. Kim, S. A.; Jeong, K.-J.; Yethiraj, A.; Mahanthappa, M. K. Low-Symmetry Sphere Packings of Simple Surfactant Micelles Induced by Ionic Sphericity. *Proc. Natl. Acad. Sci. U. S. A.* **2017,** *114*, 4072-4077.

73. Lee, S.; Leighton, C.; Bates, F. S. Sphericity and Symmetry Breaking in the Formation of Frank-Kasper Phases from One Component Materials. *Proc. Natl. Acad. Sci. U. S. A.* **2014,** *111*, 17723-17731.

74. Rappolt, M.; Cacho-Nerin, F.; Morello, C.; Yaghmur, A. How the Chain Configuration Governs the Packing of Inverted Micelles in the Cubic Fd3m-Phase. *Soft Matter* **2013,** *9*, 6291-6300.

75. Turner, D. C.; Gruner, S. M. X-Ray Diffraction Reconstruction of the Inverted Hexagonal (H_{II}) Phase in Lipid-Water Systems. *Biochemistry* **1992,** *31*, 1340-1355.

76. Anderson, D. M.; Gruner, S. M.; Leibler, S. Geometrical Aspects of the Frustration in the Cubic Phases of Lyotropic Liquid Crystals. *Proc. Natl. Acad. Sci. U. S. A.* **1988,** *85*, 5364-5368.

77. Chen, Z.; Rand, R. P. Comparative Study of the Effects of Several *n*-Alkanes on Phospholipid Hexagonal Phases. *Biophys. J.* **1998,** *74*, 944-952.

78. Weber, R. L.; Mahanthappa, M. K. Thiol-Ene Synthesis and Characterization of Lithium Bis(malonato)borate Single-Ion Conducting Gel Polymer Electrolytes. *Soft Matter* **2017,** *13*, 7633-7643.

79. Petříček, V.; Dušek, M.; Palatinus, L. Crystallographic Computing System *JANA2006*: General Features. *Z. Kristallogr.* **2014,** *229*, 345–352.

80. Palatinus, L.; Chapuis, G. *SUPERFLIP*–A Computer Program for the Solution of Crystal Structures by Charge Flipping in Arbitrary Dimensions. *J. Appl. Cryst.* **2007,** *40*, 786-790.

81. Momma, K.; Izumi, F. VESTA 3 for Three-Dimensional Visualization of Crystal, Volumetric and Morphology Data. *J. Appl. Cryst.* **2011,** *44*, 1272-1276.

82. Sobeck, D. C.; Higgins, M. J. Examination of Three Theories for Mechanisms of Cation-Induced Bioflocculation. *Water. Res.* **2002,** *36*, 527-538.

83. Liu, C. K.; Warr, G. G. Hexagonal Closest-Packed Spheres Liquid Crystalline Phases Stabilised by Strongly Hydrated Counterions. *Soft Matter* **2014,** *10*, 83-87.

84. Alexander, S.; McTague, J. Should All Crystals Be BCC? Landau Theory of Solidification and Crystal Nucleation. *Phys. Rev. Lett.* **1978,** *41*, 702-705.

85. Barauskas, J.; Cervin, C.; Tiberg, F.; Johnsson, M. Structure of Lyotropic Self-Assembled Lipid Nonlamellar Liquid Crystals and Their Nanoparticles in Mixtures of Phosphatidyl Choline and α-Tocopherol (Vitamin E). *Phys. Chem. Chem. Phys.* **2008,** *10*, 6483-6485.

86. Gibbs, W. J. On the Equilibrium of Heterogeneous Substances. *Trans. Conn. Acad. Arts Sci.* **1875-78,** *3*, 108-248.

87. Feinstein, M. E.; Rosano, H. L. The Determination of the Apparent Binding of Counterions to Micelles by Electromotive Force Measurements. *J. Colloid Interface Sci.* **1967,** *24*, 73-79.

88. Brun, T. S.; Hoiland, H.; Vikingstad, E. The Fraction of Associated Counterions and Singly Dispersed Amphiphiles in Micellar Systems from Ion Exchange Membrane Electrode Measurements. *J. Colloid Interface Sci.* **1978,** *63*, 590-592.

89. Pettitt, B. M.; Rossky, P. J. Alkali Halides in Water: Ion–Solvent Correlations and Ion–Ion Potentials of Mean Force at Infinite Dilution. *J. Chem Phys.* **1986,** *84*, 5836-5844.

90. Jho, Y. S.; Kanduč, M.; Naji, A.; Podgornik, R.; Kim, M. W.; Pincus, P. A. Strong-Coupling Electrostatics in the Presence of Dielectric Inhomogeneities. *Phys. Rev. Lett.* **2008,** *101*, 188101/1–188101/4.